communications physics

Article

https://doi.org/10.1038/s42005-024-01650-5

Bursting of condensates

Isabell Tunn [1], Grégory Beaune [2], Jennifer Tersteegen [1], Teemu Välisalmi[1], Jaakko V. I. Timonen [2], Françoise Brochard-Wyart [3] ✉ & Markus B. Linder [1] ✉

Numerous biomolecular shell-forming condensates are reported in cells and bioengineered in vitro. The relationship between the molecular structure of shell-forming condensates and their biophysical properties remains largely unexplored. To fill this gap, we characterize shell-forming condensates of bioengineered spider silk proteins based on *Araneus diadematus* major ampulla gland silk fibroin 3 (ADF3) using micropipette aspiration. We observe that condensates can burst during aspiration like soap bubbles or polymersomes, demonstrating the formation of a dense protein layer (shell) at the condensate interface. The tendency to burst is more pronounced for condensates formed from proteins with weakly dimerizing terminal blocks. We develop a model to analyse the aspiration and bursting of the condensates, to obtain the surface and bulk viscosity, and to estimate the shell thickness and viscosity. Understanding and controlling the bursting of condensates will open avenues for their use in materials, as compartments for reactions or drug delivery systems.

Biomolecular condensates—also known as coacervates—are formed by the physical process of liquid-liquid phase separation (LLPS) resulting in a dense condensate phase and a dilute phase. Condensates have crucial functions as membraneless organelles in cells[1,2] and for the storage of proteinaceous material building blocks that form high performance extracellular biomaterials such as sandcastle worm cement, squid beak, mussel byssus threads, and velvet worm slime[3,4]. Knowledge of the biophysical properties of condensates will aid in tuning their stability for material formation processes, drug release, and their use as dynamic compartments for biochemical reactions.

To date a wide variety of techniques[5], i.e., coalescence studies, fluorescence recovery after photobleaching, fluorescence correlation spectroscopy, active and passive micro-rheology, and micropipette aspiration[6], are available to study the biophysical properties of condensates. In this work, we characterized a set of five condensate-forming spider silk proteins using micropipette aspiration as a label-free technique. Using light microscopy, we monitor the aspiration of the condensate when a step suction pressure is applied with a micrometric glass pipette filled with the dilute phase, followed by the retraction of the condensate when the pressure is released[6,7]. We often observed bursting of the condensates during aspiration, indicating that they have a shell.

Bursting of liquid shells can be observed in everyday life with soap and viscous bubbles because suspended films are always unstable. At the microscopic scale, vesicles and polymersomes are stable, but burst when the membrane is put under tension either by adhesion to a substrate[8], during micropipette aspiration[9,10], in electric fields[11,12], or induced by ultraviolet (UV) light[13,14]. Mabrouk et al.[13] engineered asymmetric polymersomes that burst upon exposure to UV light due to the structural rearrangement of an azobenzene group containing block copolymer in the outer leaflet. Polymersome bursting was initiated by the nucleation of a pore followed by membrane curling at the pore edge to relax the stored curvature energy. The membrane thickness in polymersomes can vary from 1–21 nm depending on the block copolymers used[15–17].

Homogeneous spherical droplets are the most observed topology of biomolecular condensates since they are formed by phase separation. However, a wide variety of complex structures have recently been discovered, such as vesicles, "shell condensates" or core-shell condensates consisting of two or more distinct concentric layers of biomolecules, polymers or surfactants packed like nested "Russian dolls"[18]. Several theoretical approaches have been developed to describe the wide variety of condensate morphologies, which can be divided into two classes: active systems and passive systems. In active systems, it has been shown theoretically and experimentally that condensates forming liquid spherical shells are a non-equilibrium steady state of active droplets[19–21]. Droplets can undergo spinodal instability and form stationary shells. This structure, which is unstable due to capillarity, is kept out of equilibrium by chemical reactions. In passive systems, shell structures are formed by free energy minimization due to self-organization or phase transition of proteins. While the physics of liquid mixtures with a few components (binary or ternary) is well understood, the phase behavior of mixtures with a number of components $N > 3$, which is a common case for proteins of intracellular fluids, has only recently been studied[18]. Spherical shells can be formed from three phases that coexist like

[1]Department of Bioproducts and Biosystems, Aalto University School of Chemical Engineering, Espoo, Aalto FI-00076, Finland. [2]Department of Applied Physics, Aalto University School of Science, Espoo, Aalto FI-00076, Finland. [3]Institute Curie, Université Paris Sciences et Lettres, Sorbonne Université, CNRS UMR168, Laboratoire Physico Chimie Curie, Paris 75005, France. ✉e-mail: Francoise.Brochard@curie.fr; Markus.Linder@aalto.fi

"Russian doll droplets", where a phase I droplet is immersed in a phase II droplet that is itself surrounded by a phase III droplet. If the surface tension inequalities are satisfied, these shells are stable and do not burst. This can explain many intracellular core-shell condensates, such as paraspeckles[22], nucleoli[23] and TDP-43 HSP70 anisosomes[24], or bioengineered core-shell coacervates consisting of RNA and protein[25,26].

However, this does not apply to our system where $N = 2$. Our interpretation is that amphiphilic spider silk proteins with alternating hydrophobic alanine-rich and hydrophilic glutamine-rich stretches are adsorbed in a dense layer at the interface between the dense and dilute phases. The adsorption reduces the protein concentration in the condensate. Another cause could be protein structural transition, which alters the balance of intermolecular forces between proteins[27]. The net result is a decrease in protein concentration and the droplet could become unstable by spinodal decomposition[28] below a critical concentration given by the spinodal curve. Subsequent internal phase separation induced by a decrease in concentration has been proposed to explain the evolution of a spherical plain into a vesicle-like condensate[29]. This instability leads to the formation of the shell of thickness much greater than the molecular sizes. The internal concentration of the condensate can be either equal to the concentration of the dilute phase when the droplet becomes unstable or greater when the droplet remains stable. Similar to viscous bubbles, these shell condensates are metastable and burst by nucleation and growth of a hole. In summary, both active and passive systems can lead to shell condensates. The reported shell thickness for condensates is in the range of 0.5–2 μm[29–31].

Shell-forming condensates have not been studied with micropipette aspiration, which applies a suction pressure that may induce bursting. Here, we develop a model to extract a broad range of rheological properties such as the surface tension, the surface viscosity, and the bulk viscosity of bursting condensates. The fusion of these condensates cannot be described by the classical Frenkel law[32], as it does not consider the presence of a shell. We investigate the effect of the mid- and terminal blocks of the spider silk proteins on the biophysical properties and the tendency to burst. The surface tension of the condensates ranged from 3–19 μN m^{-1} and the bulk viscosity was 0.5–20 Pa·s depending on the protein used and the protein concentration in the range of millimolar. The surface viscosity of the condensate shell was 9–68 μN s m^{-1} and the shell thickness was estimated to be in the range of 100–300 nm. The shell viscosity ranged from 40–250 Pa·s. A dimerization strength of the terminal blocks in the micromolar to millimolar range and a native spider silk midblock promote condensate bursting, indicating that they are more fragile. The protein shell of the passive condensates may be based on the adsorption of the amphiphilic spider silk protein phase in different conformations and via hydrophobic interactions leading to a dense coating at the interface between the dense and dilute phases. The bursting of the spider silk condensates may be tunable by factors such as protein concentration, pH, salts, or pressure which control the phase diagram, i.e., the coexistence and the spinodal curves.

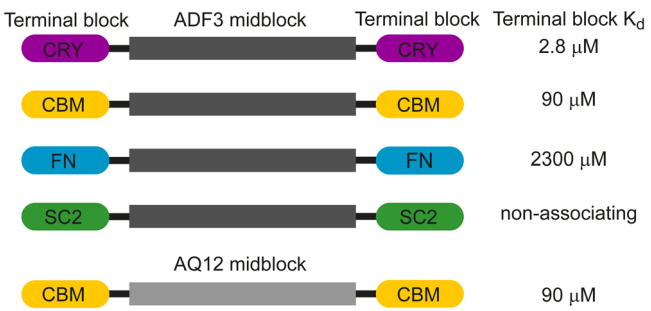

Fig. 1 | Scheme of spider silk proteins. All proteins consist of two globular terminal blocks connected by a short linker to the repetitive silk midblock. The terminal blocks are γD-crystallin (CRY), cellulose binding module (CBM), fibronectin III domain 10 (FN), and version 2 of SpyCatcher (SC2). The midblocks are the spider silk fibroin ADF3 and its engineered version AQ12. The dissociation constant K_d of the terminal blocks was determined by AUC[43]. Full protein sequences are available in the Supplementary Data 1.

Results

Engineered spider silk proteins

To investigate the effect of the terminal and midblock of the spider silk proteins on the biophysical properties and bursting of the condensates, five sequences were compared in this work. The proteins studied consist of a globular terminal block at the N- and C-terminus and a highly repetitive midblock spaced by short linkers (Fig. 1). Previous work indicates that the terminal block interactions act as main contributors to facilitate the stability and cohesion of the condensates[33]. The intrinsically disordered midblock provides a secondary contribution to the condensate stability via multivalent weak interactions[33]. The two midblocks used were the major ampulla gland silk fibroin 3 from *Araneus diadematus*[34,35] (molecular weight (MW) = 43.0 kDa) and an engineered version of *A. diadematus* fibroin 3 (ADF3) with 12 repeat units[36] (AQ12, MW = 46.5 kDa). The midblocks are highly repetitive and have alanine- (Ala) and glutamine- (Gln)-rich stretches. The globular proteins γD-crystallin (CRY) from *Homo sapiens*[37], cellulose binding module (CBM) from *Ruminiclostridium thermocellum*[38], fibronectin III domain 10 (FN) from *H. sapiens*[39] and version 2 of SpyCatcher (SC2)[40,41] were used as terminal blocks (sequences in Supplementary Data 1)[42]. The terminal blocks are similar in molecular weight and structure. However, they differ in their dimerization strength and their binding mode, e.g., SC2 terminal blocks do not associate because of charge repulsion while FN end blocks can associate via dipole-dipole interactions[43]. The terminal block dissociation constant K_d was found to be correlated to the tendency of the silk proteins to form condensates[43]. The dissociation constant K_d defines the propensity of two or more molecules to reversibly dissociate into single components. The K_d of each terminal block was determined by analytical ultracentrifugation (AUC) by ref. 43 (Fig. 1). All proteins were recombinantly expressed in *Escherichia coli* and purified. As a final step a buffer exchange to water was performed. The purity and identity of the proteins was confirmed by sodium dodecyl sulphate polyacrylamide gel electrophoresis (Supplementary Fig. 1). Condensates were formed by LLPS when protein concentration was increased by removing water in centrifugal concentrator units (Methods: *Condensate formation*).

Aspiration and bursting of condensates

Micropipette aspiration is a well-suited technique measuring the mechanical properties of soft objects, from liquid droplets to vesicles or capsules, such as polymersomes. The spider silk proteins studied here can form condensates by LLPS when increasing the protein concentration. A micrometric borosilicate pipette filled with dilute phase was used to aspirate the spider silk condensates with suction pressures ΔP of 4–100 Pa, followed by retraction of the condensates when the pressure was released ($\Delta P = 0$ Pa). Unexpectedly, aspiration often led to the bursting of CBM-ADF3-CBM, FN-ADF3-FN, and SC2-ADF3-SC2 condensates. Figure 2 shows the aspiration, retraction, and bursting of a CBM-ADF3-CBM condensate. Bursting often starts from a defect, i.e., the pipette or small solid precipitates inside the condensate. Small solid precipitates inside the condensates and in the dilute phase are present even in a freshly prepared sample (Fig. 2).

The tendency to burst appears to be sensitive to the architecture of the proteins. No bursting events were observed for CRY-ADF3-CRY (Supplementary Movie 1). For CBM-ADF3-CBM (Supplementary Movie 2) all condensates that were aspirated did burst, whereas for FN-ADF3-FN (Supplementary Movie 3, 4) and SC2-ADF3-SC2 (Supplementary Movie 5, 6) both non-bursting and bursting condensates were aspirated in the same sample.

The bursting of the condensates demonstrates that the protein concentration is not homogeneous throughout the condensate but forms a dense layer (shell) on the surface. In that case, the micropipette aspiration will lead to a measurement of the surface tension and surface viscosity of the shell[13,44]. The shell could be formed by adsorption of spider silk proteins at

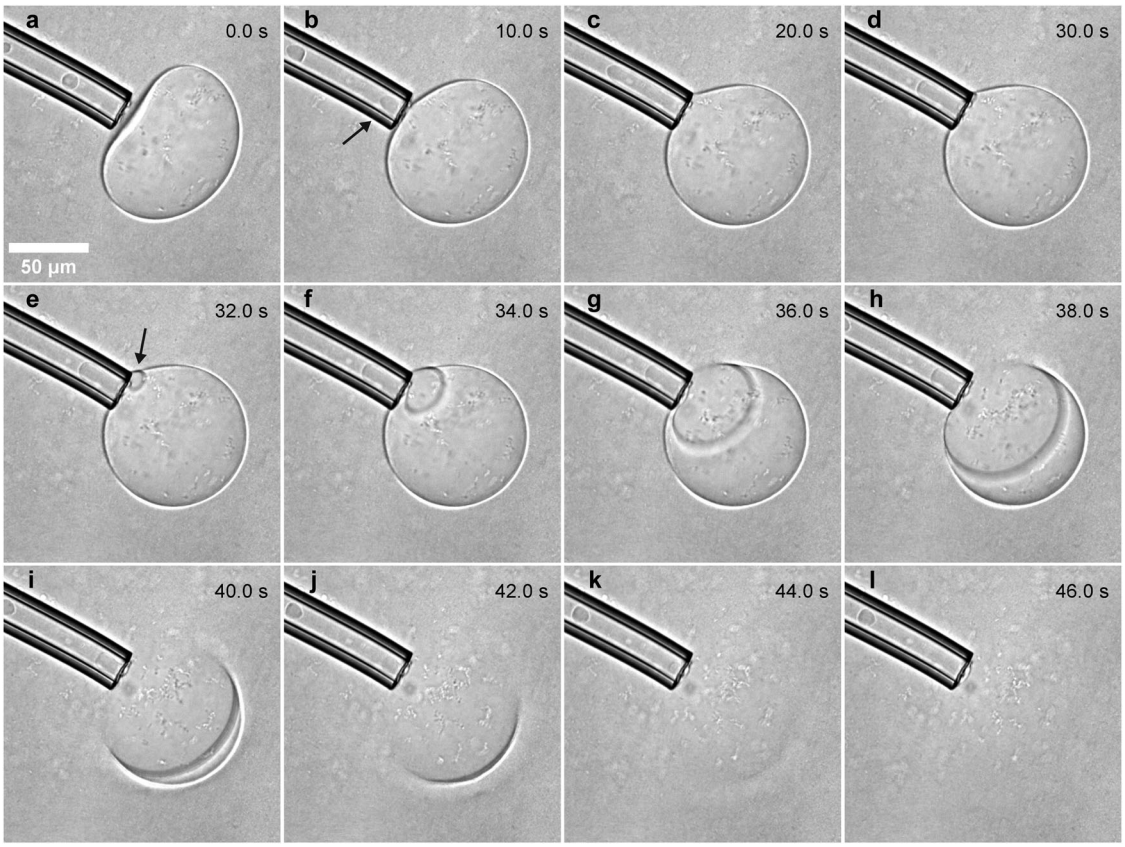

Fig. 2 | Aspiration followed by bursting of a CBM-ADF3-CBM condensate. **a**–**c** Aspiration of the condensate with $\Delta P = 5$ Pa. Arrow in (**b**) indicates the aspiration front. **d**–**l** Retraction, no applied pressure. **e**–**l** Bursting of the condensate initiated at the site of aspiration. The arrow in (**e**) indicates the site of bursting. The silk proteins tend to form small solid precipitates inside the condensates and in the dilute phase. Scale bar: 50 µm.

the interface between the dense and dilute phase coupled to a thermodynamic instability.

Condensates can undergo coalescence during the micropipette experiment (Supplementary Fig. 2). CRY-ADF3-CRY, CBM-ADF3-CBM and FN-ADF3-FN condensates are still present 10 days after preparation (Supplementary Fig. 3) and CBM-AQ12-CBM condensates are still present 36 days after sample preparation (Supplementary Fig. 4). SC2-ADF3-SC2 condensates seem to be in a glassy state and show no coalescence after 1 day and contain only precipitates after 2 days. LLPS of SC2-ADF3-SC2 is based on the multivalent weak interactions of the amphiphilic spider silk midblock, which seems to lead to faster formation of glassy condensates and precipitates. In contrast, CRY-ADF3-CRY, CBM-ADF3-CBM, and FN-ADF3-FN condensates can coalesce after 7 days. However, the coalescence time increases for CRY-ADF3-CRY condensates after 2 days and they do not coalesce after 10 days, indicating that they become more viscous. CBM-ADF3-CBM and FN-ADF3-FN condensates are coalescing similarly fast after 10 days as on the day of sample preparation. CBM-AQ12-CBM condensates can undergo coalescence and are liquid up to 22 days after sample preparation, indicating that the time stability of the condensates depends on the terminal blocks and the midblock (Supplementary Figs. 5 and 6).

Analysis of aspiration and bursting of condensates

The surface tension γ and the surface viscosity η_s of the condensates were determined from the aspiration and retraction using a micropipette (Fig. 3a). A shell of thickness e and viscosity η_m delimits the condensate. We assume that the protein solution inside and outside the condensate have different concentrations with a bulk viscosity η_b and a dilute phase viscosity η^*_b (Fig. 3b). When applying suction pressure during aspiration, we observe either immediate bursting or the formation of a tongue, followed by the bursting by nucleation and growth of a hole of radius $r(t)$ (Fig. 3c, d). We can also observe the formation of a rim which collects the liquid of the hole (Figs. 3c and 4).

When a suction pressure ΔP is applied above a critical threshold pressure ΔP_c, the condensate with radius R_0 enters the pipette (radius R_p) forming a tongue of length L (Fig. 3a). The driving force F_M

$$F_M = \pi R_p^2(\Delta P - \Delta P_c) \tag{1}$$

where the critical pressure ΔP_c is derived from the Young-Laplace law[45], assuming a non-wetting liquid. For plain condensates without shell, $\Delta P_c = 2\gamma(\frac{1}{R_p} - \frac{1}{R_0})$, but for condensates with a shell there are two interfaces and

$$\Delta P_c = 4\gamma\left(\frac{1}{R_p} - \frac{1}{R_0}\right) \tag{2}$$

Equation (2) assumes a non-wetting regime with a convex hemispherical meniscus. The dynamics of aspiration $L(t)$ results from a balance between F_M and the friction force F_v. The friction force F_v is different for plain versus condensates with a shell. For plain condensates of viscosity η_b, $F_v = c\eta_b R_p \dot{L}$ where the numerical factor $c = 3\pi^2$ has been calculated analytically[46] and demonstrated experimentally by Piroird et al.[47].

For condensates with a liquid shell separating the interior and exterior, F_v was first calculated by Needham et al. for vesicles[48], assuming that the viscous dissipation is dominated by the flow of the membrane into the capillary and that the slippage of the membrane

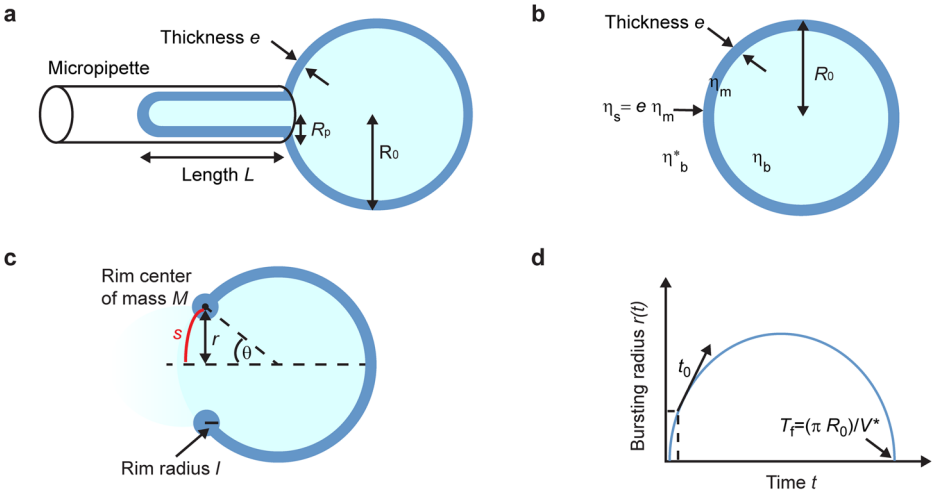

Fig. 3 | Data analysis of non-bursting and bursting spider silk condensates. a Scheme of the aspiration of a condensate with radius R_0, shell thickness e using micropipette aspiration with the pipette radius R_p. **b** Schematic of a condensate with bulk viscosity η_b, dilute phase viscosity η^*_b, surface viscosity η_s and shell viscosity η_m. **c** Schematic of the bursting of the condensate with the opening angle θ and the bursting radius r ($r = R_0 \sin\theta$). The forming liquid rim has a center of mass M and radius l. The curvilinear coordinate is $s = R_0\theta$. **d** Schematic plot of the bursting radius $r(t)$ versus time with the final time point $T_f = \pi R_0/V^*$ with the bursting velocity V^*.

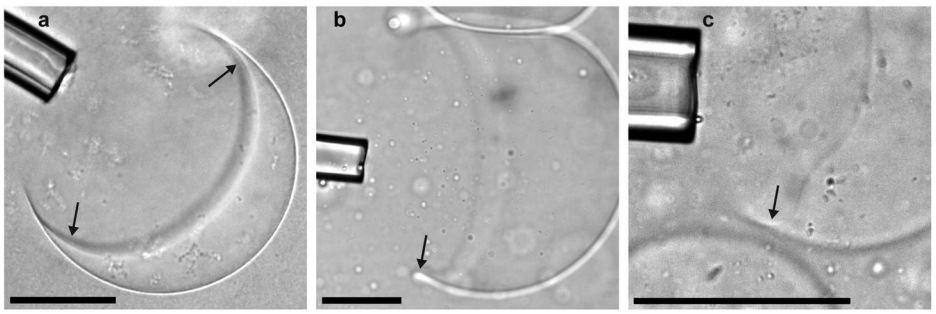

Fig. 4 | Rim formation during condensate bursting. Representative image of (**a**) CBM-ADF3-CBM, (**b**) FN-ADF3-FN, and (**c**) SC2-ADF3-SC2 condensate during bursting. Arrows pointing at positions where the cylindrical rim is visible. Scale bar: 50 µm.

in the pipette is negligible. This can be verified if the condensate is sucked inside the pipette and a small ΔP is applied.

$$F_v = 4\pi\eta_s \dot{L}\left(1 - \frac{R_p^2}{R_0^2}\right) \tag{3}$$

Where $\eta_s = \eta_m e$ is the surface viscosity of the shell of thickness e. The balance of forces leads to an aspiration velocity $\dot{L}_a$:

$$\dot{L}_a = \frac{R_p^2}{4\eta_s}\left(\Delta P - \Delta P_c\right) \tag{4}$$

assuming that $R_p \ll R_0$. (Fig. 5a). When $\Delta P = 0$ (Fig. 5b), the tongue in the micropipette retracts with a velocity $\dot{L}_r$ given by

$$\dot{L}_r = \frac{R_p^2}{4\eta_s}\Delta P_c \approx \frac{\gamma}{\eta_s}R_p = \frac{R_p}{\tau_m^*} \tag{5}$$

where $1/\tau_m^*$ is a capillary frequency which characterizes the wetting of the condensate, in analogy with the capillary velocity for the wetting of plain condensates. Experimentally ΔP_c was calculated from the aspiration and retraction velocity:

$$\Delta P_c = \Delta P \frac{\dot{L}_r}{\dot{L}_r + \dot{L}_a} \tag{6}$$

Then Eq. (4) was used to obtain the surface viscosity η_s (Fig. 5a, Supplementary Figs. 7–12). Data are reported with the standard error of mean (SEM) and the number of condensates n. We performed a Wilcoxon signed-rank test with a significance threshold of $p < 0.05$, assigning a rank letter (e.g., a, b, c) to each protein. To illustrate, a dataset marked with rank 'a' is significantly different from datasets marked with ranks 'b' or 'c'. When the assigned rank is 'ab', the dataset is not significantly different from those with ranks 'a' or 'b'. The exact p values, confidence intervals and effect sizes are available in Supplementary Data 2. CBM-ADF3-CBM and FN-ADF3-FN condensates have a similar η_s (9.2 ± 1.3 µN s m^{-1} ($n = 9$, rank = a) and 9.3 ± 1.7 µN s m^{-1} ($n = 15$, rank = a) respectively). The surface viscosity was 59.4 ± 17.4 µN s m^{-1} ($n = 11$, rank = ab) for CRY-ADF3-CRY, 67.9 ± 40.1 µN s m^{-1} ($n = 24$, rank = ab) for SC2-ADF3-SC2 and 52.2 ± 9.3 µN s m^{-1} ($n = 17$, rank=b) for CBM-AQ12-CBM (Table 1). The high η_s of SC2-ADF3-SC2 with the non-associating SC2 terminal blocks indicates that the multivalent interactions of the midblock are crucial for the condensate properties. The Wilcoxon test further shows a difference in η_s between CBM-ADF3-CBM and CBM-AQ12-CBM.

We use Eqs. (2) and (6) to calculate the surface tension ranging from 3.4 ± 0.7 µN m^{-1} ($n = 9$, rank = a) for CBM-ADF3-CBM to 17.4 ± 3.4 µN m^{-1} ($n = 20$, rank = b) for SC2-ADF3-SC2 (Table 1). The critical pressure and therefore the surface tension could not be obtained for bursting condensates of FN-ADF3-FN and SC2-ADF3-SC2 since they burst before retraction. In this case, the mean surface tension of the condensates that did not burst was taken for further calculations. The surface tension of the non-bursting FN-ADF3-FN (rank=ab) and SC2-ADF3-SC2 (rank=b) condensates is 4-5 times higher than for CBM-ADF3-CBM (rank=a) condensates and indicates that the condensates are more cohesive. The energy of nucleation of a hole in a shell is inversely proportional to the shell surface tension. This explains why they burst early during retraction. The mean capillary frequency is similar for CBM-ADF3-CBM (0.38 ± 0.07 s^{-1} ($n = 9$, rank=b)), SC2-ADF3-SC2 (0.94 ± 0.42 s^{-1} ($n = 24$, rank=ab)), and CBM-AQ12-CBM (0.50 ± 0.10 s^{-1} ($n = 17$, rank=b)) (Table 1). For CRY-ADF3-

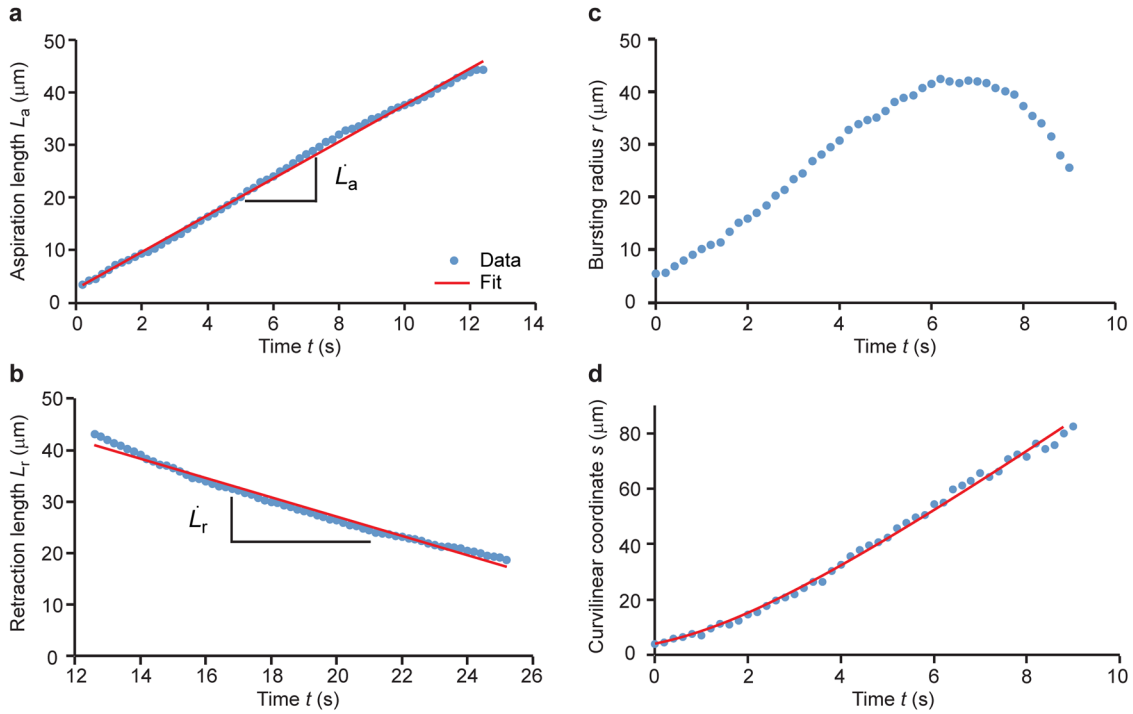

Fig. 5 | Representative data set for a CBM-ADF3-CBM condensate. a Aspiration curve, (**b**) Retraction curve, (**c**) Bursting radius *r(t)* and (**d**) Curvilinear coordinate plot for a representative CBM-ADF3-CBM condensate. Data points are depicted as blue circles. The red lines are the fits to extract the aspiration (linear fit: $L_a = \dot{L}_a t + n$), retraction (linear fit: $L_r = -\dot{L}_r t + n'$) and bursting velocities (Eq. 16), respectively.

CRY the capillary frequency is only 0.20 ± 0.03 s^{-1} (n = 11, rank=a). For FN-ADF3-FN the capillary frequency is 2.31 ± 0.42 s^{-1} (n = 15, rank=c).

Model of bursting of condensates

We model the dynamics of bursting of condensates *r(t)* using an analogy with two cases theoretically described by one of us[49–51]. The first case corresponds to the bursting of ultra-viscous polymer films and bubbles studied by Debregeas et al.[49,50]. The film remains flat, *r(t)* increases exponentially, and no rim is formed around the hole. In the second case, ref. 51 studied the dewetting of a liquid film deposited on a liquid bath. In this case, the hole is surrounded by a liquid rim and opening radius of the hole r increases linearly with time.

In the case of shell-forming condensates, the film is embedded in a viscous medium, whereas for the bursting of bubbles the medium is air. We will show that the friction with the external viscous protein solution gives rise to the formation of a rim. At short times, we can expect an exponential growth when the dissipation in the film dominates and at long times the formation of a rim. The model we developed is valid for all condensates that have a shell, including hollow and core-shell condensates. In case of core-shell condensates where the medium viscosity is different inside and outside the more viscous medium will dominate the friction[13].

We model the dynamics of bursting from a transfer of surface energy into viscous dissipation. The gain in surface area is proportional to the dewetted area A corresponding to the spherical cap bounded by the hole.

$$A = 2\pi(1-\cos\theta)R_0^2 \tag{7}$$

Where θ is the angular coordinate of the rim. The radius l of the rim collecting the liquid of the hole is given by the mass conservation equation:

$$Ae = 2\pi^2 rl^2 \tag{8}$$

In the limit of $r < R_0$ and $\theta \ll \pi/2$,
$1-\cos\theta \approx \frac{1}{2}\theta^2, A \approx \pi r^2$, and the cylindrical rim radius l becomes $l = \sqrt{\frac{er}{2\pi}}$

In the limit of $r < R_0$, we can neglect the curvature of the film. The gain of surface energy $2\gamma A$, dissipated by both the friction with the surrounding liquid and the intrinsic dissipation inside the film, can be written as:

$$2\gamma\frac{dA}{dt} = 4\gamma\pi r\dot{r} = 4\pi\eta_s\dot{r}^2 + 2\pi\widetilde{\eta}_b r\dot{r}^2 \tag{9}$$

where $A \approx \pi r^2, \dot{r} = \frac{dr}{dt}, \widetilde{\eta}_b = \frac{4\pi\eta_b}{\ln\frac{2\pi r}{l}} \sim \eta_b$, where η_b is the bulk viscosity and $\eta_s = \eta_m e$ is the surface viscosity.

The first term describes the gain of surface energy. The second term is the plug flow dissipation inside the film associated to the radial flows generated by the hole opening. The plug flow dissipation inside the film was first introduced in the bursting of ultra-viscous films and bubbles[49,52] and the opening of pores in stretched vesicles[53].The third term is associated with the Stokes friction exerted by the surrounding liquid on the rim of radius l moving at velocity $\dot{r}$ assuming a plug flow in the rim[45]. It was introduced to describe the liquid/liquid dewetting[51,54] and the bursting of light sensitive polymersomes[13].

The comparison of the two energy dissipation terms leads to a cross-over radius r_c

$$r_c = 2\frac{\eta_s}{\widetilde{\eta}_b} = 2e\frac{\eta_m}{\widetilde{\eta}_b} \tag{10}$$

The integration of Eq. (9) leads to:

$$V^* t = r - r_i + r_c \ln\left(\frac{r}{r_i}\right) \tag{11}$$

where $V^* = \frac{2\gamma}{\widetilde{\eta}_b}$ and r_i is the initial radius of the hole at $t = 0$.

Equation (11) shows that at short times *r(t)* increases exponentially (Fig. 5c) up to $r = r_c$ corresponding to the formation of the rim. We notice an analogy with the dewetting of an ultra-viscous polymer film deposited on a solid substrate, where the friction with the substrate leads to the formation of

a rim[50]. Above r_c, r increases linearly with time. The velocity of bursting $\dot{r} = \frac{dr}{dt}$ is given by $\dot{r} = V^*$.

Equation (11) is limited to the early stage of bursting assuming $r < R_0$. To describe the full opening, we introduce the curvilinear coordinate s (Figs. 3d, 5d).

$$s = R_0\theta \tag{12}$$

The energy balance between the gain of surface energy and viscous dissipation both on the rim and inside the film is now:

$$2\gamma\frac{dA}{dt} = 4\gamma\pi r\frac{ds}{dt} = 4\pi\eta_s\left(\frac{ds}{dt}\right)^2 + \widetilde{\eta}_b 2\pi r\left(\frac{ds}{dt}\right)^2 \tag{13}$$

where $r = R_0\ sin\ \theta$. As soon as r is larger than r_c, the last term is dominant, and the solution of Eq. (13) is simply:

$$\frac{ds}{dt} = V^* \tag{14}$$

leading to $\theta = \frac{V^*}{R_0}t$,

$$r = R_0\sin\left(\frac{2\gamma t}{\widetilde{\eta}_b R_0}\right) = R_0\sin\left(\frac{V^*}{R_0}t\right) \tag{15}$$

This sinusoidal expression for the opening describes well that $r(t)$ increases until $r(t) = R_0$ and decreases to zero when the bursting is complete but is only valid for $r > r_c$ (Fig. 3d).

The general expression for the curvilinear coordinate $s(t)$ solution of Eq. (13) is

$$V^*t = s - s_i + r_c\ln\left(\frac{s}{s_i}\right) \tag{16}$$

where s_i is the curvilinear coordinate at $t = 0$. The mean values for s_i are 5.4 ± 0.6 μm ($n = 9$) for CBM-ADF3-CBM, 19.9 ± 4.4 μm ($n = 7$) for FN-ADF3-FN and 23 ± 4.1 μm ($n = 4$) for SC2-ADF3-SC2. The curvilinear coordinate $s(t)$ increases exponentially at short times and linearly when s becomes larger than r_c. The fit of Eq. (16) to the data for $s(t)$ was used to obtain V^* and r_c (Fig. 5d).

Using the definition of V^*, one can calculate the bulk viscosity of 0.5 ± 0.1 Pa·s ($n = 9$, rank=a) (mean ± SEM) for CBM-ADF3-CBM (total protein concentration c = 0.6 mM), 0.7 ± 0.1 Pa·s ($n = 7$, rank=a) for FN-ADF3-FN (c = 1.1 mM) and 20.3 ± 3.3 Pa·s ($n = 4$, rank=b) for SC2-ADF3-SC2 (c = 1.1–1.4 mM) (Table 1). The Wilcoxon signed-rank test indicates that η_b is significantly higher in SC2-ADF3-SC2 compared to CBM-ADF3-CBM and FN-ADF3-FN ($p < 0.05$). Figure 6 shows the box plots of the calculated values for the surface viscosity (Fig. 6a), bulk viscosity (Fig. 6b), shell viscosity (Fig. 6c), surface tension (Fig. 6d), capillary frequency (Fig. 6e) and the shell thickness (Fig. 6f) of all proteins. All data used in Fig. 6 are in Supplementary Data 3. The plot of $s(t)$ shows an initial exponential growth until the birth of the rim followed by a linear increase (Fig. 5d, Supplementary Fig. 9c, Supplementary Fig. 11c). The mean values of r_c are comparable for all condensates at 19.2 ± 6.0 μm ($n = 9$) for CBM-ADF3-CBM, 20.1 ± 8.8 μm ($n = 7$) for FN-ADF3-FN and 21.5 ± 8.5 μm ($n = 4$) for SC2-ADF3-SC2 (mean ± SEM) (Table 1).The r_c values obtained from fitting Eq. (16) can be used to calculate an a-dimensional plot of the curvilinear coordinate $s^*(t^*)$ (Eq. (17)).

$$t^* = s^* - s_i^* + \ln\left(\frac{s}{s_i}\right) \tag{17}$$

Where $t^* = t/\tau$, with $\tau = r_c/V^*$ and $s^* = s/r_c$. The dimensionless plot of $s^*(t^*)$ shows that all bursting events for a given protein lie on a single master curve even if they have different values for r_c and V^* (Fig. 7a, c).

Table 1 | Biophysical properties of non-bursting and bursting condensates

Protein	Surface tension γ (μN m^{-1})	Bulk viscosity η_b (Pa s)	Surface viscosity η_s (μN s m^{-1})	Capillary frequency γ/ η_s (s^{-1})	Cross-over radius R_c (μm)	Shell thickness e (nm)	Shell viscosity η_m (Pa s)	Concentration (mM)
CRY-ADF3-CRY	10.4 ± 2.8 ($n = 11$)	-	59.4 ± 17.4 ($n = 11$)	0.20 ± 0.03 ($n = 11$)	-	-	-	1.3–1.7
CBM-ADF3-CBM	3.4 ± 0.7 ($n = 9$)	0.5 ± 0.1 ($n = 9$)	9.2 ± 1.3 ($n = 9$)	0.38 ± 0.07 ($n = 9$)	19.2 ± 6.0 ($n = 9$)	220 ± 60 ($n = 9$)	42.5 ± 5.8 ($n = 9$)	0.6
FN-ADF3-FN	14.1 ± 2.6 ($n = 8$)[a]	0.7 ± 0.1 ($n = 7$)	9.3 ± 1.7 ($n = 15$)	2.31 ± 0.42 ($n = 15$)	20.1 ± 8.8 ($n = 7$)	270 ± 80 ($n = 7$)	89.9 ± 56.8 ($n = 7$)	1.1
SC2-ADF3-SC2	17.4 ± 3.4 ($n = 20$)[a]	20.2 ± 3.3 ($n = 4$)	67.9 ± 40.1 ($n = 24$)	0.94 ± 0.39 ($n = 24$)	21.5 ± 8.5 ($n = 4$)	80 ± 10 ($n = 4$)	245.9 ± 129.6 ($n = 4$)	1.1–1.4
CBM-AQ12-CBM	19.1 ± 2.2 ($n = 17$)	-	53.2 ± 9.3 ($n = 17$)	0.50 ± 0.10 ($n = 17$)	-	-	-	n.d.

Mean ± standard error of the mean (SEM). Number of condensates measured in brackets. For bursting condensates the bulk viscosity and for non-bursting condensates the surface viscosity are given in column 2 and 3. Values for the shell thickness e and viscosity η_m are estimated from the data from measuring the rim radius and the angular coordinate. N.d.= not determined. All values are available in Supplementary Data 2.
[a]Mean surface tension of non-bursting condensates taken for further calculations because ΔP_c could not be measured for the bursting condensates.

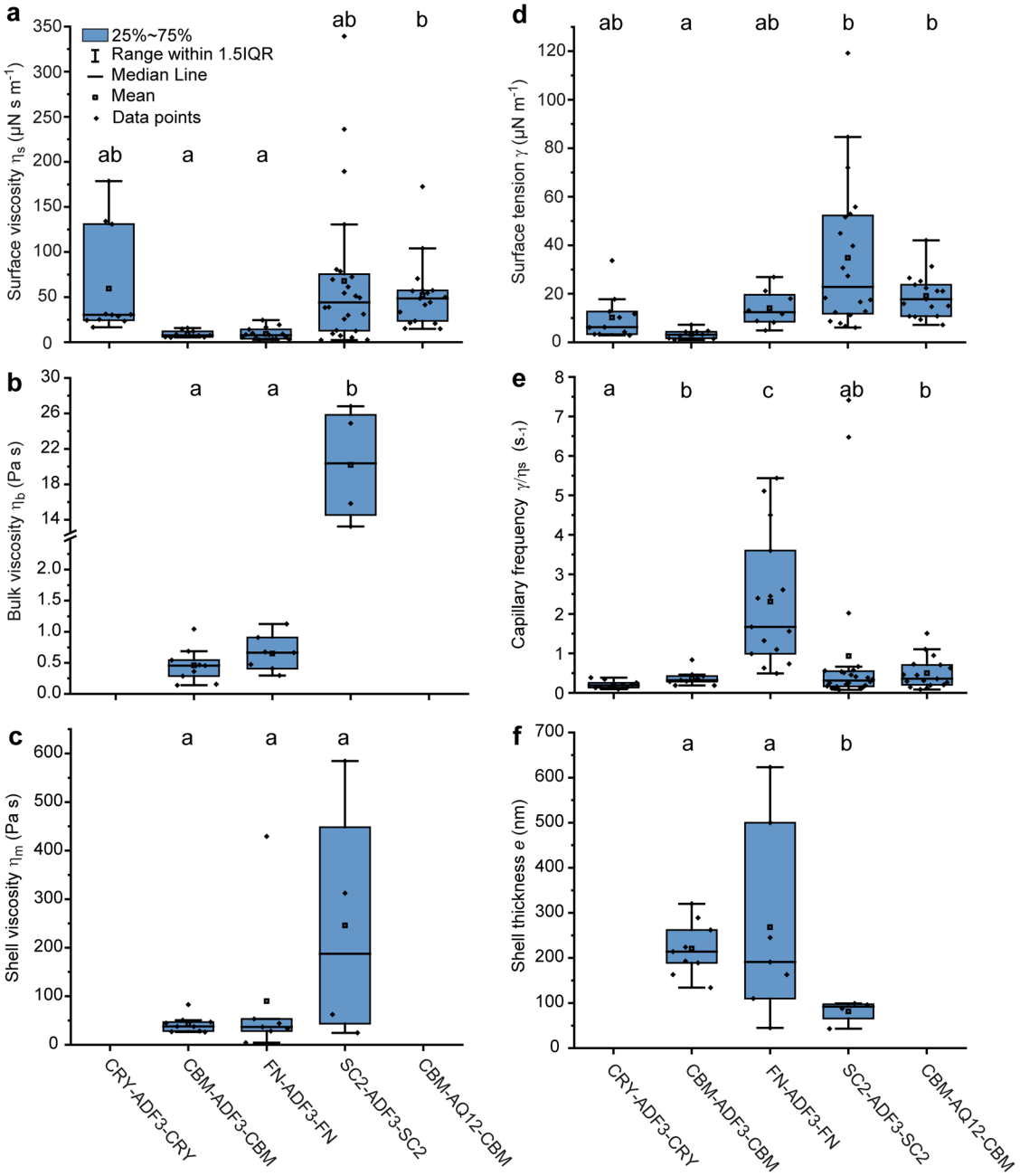

Fig. 6 | Biophysical properties of condensates. a Surface viscosity of the condensates obtained from the aspiration flow rate (Eq. (4)). The number of condensates analysed is $n = 11$ for CRY-ADF3-CRY, $n = 9$ for CBM-ADF3-CBM, $n = 15$ for FN-ADF3-FN, $n = 24$ for SC2-ADF3-SC2 and $n = 17$ for CBM-AQ12-CBM. **b** Bulk viscosity of bursting condensates calculated using the bursting velocity V^* (Eq. (11)). The bulk viscosity of CRY-ADF3-CRY and CBM-AQ12-CBM could not be determined due to the lack of analysable bursting data. The number of condensates analysed is, $n = 9$ for CBM-ADF3-CBM, $n = 7$ for FN-ADF3-FN, and $n = 4$ for SC2-ADF3-SC2. **c** Shell viscosity calculated using $\eta_s = \eta_m e$. The number of condensates analysed is $n = 9$ for CBM-ADF3-CBM, $n = 7$ for FN-ADF3-FN, and $n = 4$ for SC2-ADF3-SC2. **d** Surface tension obtained using the Young-Laplace equation (Eq. (2)). The number of condensates analysed is $n = 11$ for CRY-ADF3-CRY, $n = 9$ for CBM-ADF3-CBM, $n = 8$ for FN-ADF3-FN, $n = 20$ for SC2-ADF3-SC2 and $n = 17$ for CBM-AQ12-CBM. **e** Capillary frequency calculated using Eq. (5). The number of condensates analysed is $n = 11$ for CRY-ADF3-CRY, $n = 9$ for CBM-ADF3-CBM, $n = 15$ for FN-ADF3-FN, $n = 24$ for SC2-ADF3-SC2 and $n = 17$ for CBM-AQ12-CBM. **f** Shell thickness calculated from the estimated rim radius and the angular coordinate (Eqs. (7), (8)). The number of condensates analysed is $n = 9$ for CBM-ADF3-CBM, $n = 7$ for FN-ADF3-FN, and $n = 4$ for SC2-ADF3-SC2. The compact letter display is the result of the Wilcoxon signed-rank test with $p < 0.05$. IQR= interquartile range. Data points are displayed as black diamonds.

Furthermore, Fig. 7d confirms that the bursting process is independent of the protein used.

The thickness of the protein shell cannot be inferred from the dynamics of bursting because we do not have a measure of the shell viscosity η_m. Fortunately, we can estimate e from the size of the cylindrical rim around the hole (Fig. 4). We measured the radius of the rim at an angular coordinate of 70–95° and calculated e using Eqs. (7) and (8) which gives $(1 - \cos\theta)R_0^2 e = r\pi l^2$ with $r = R_0 \sin\theta$. The mean value for e was 220 ± 60 nm ($n = 9$, rank=a) for CBM-ADF3-CBM, 270 ± 80 nm ($n = 7$, rank=a) for FN-ADF3-FN and 80 ± 10 nm ($n = 4$, rank=b) for SC2-ADF3-SC2 (Table 1). Using these values for the shell thickness, η_m can be estimated with $\eta_s = \eta_m e$ giving 42.5 ± 5.8 Pa s ($n = 9$, rank=a) for CBM-ADF3-CBM, 89.9 ± 56.8 Pa s ($n = 7$, rank=a) for FN-ADF3-FN and 245.9 ± 129.6 Pa s ($n = 4$, rank=a) for SC2-ADF3-SC2 (Table 1). The results from the

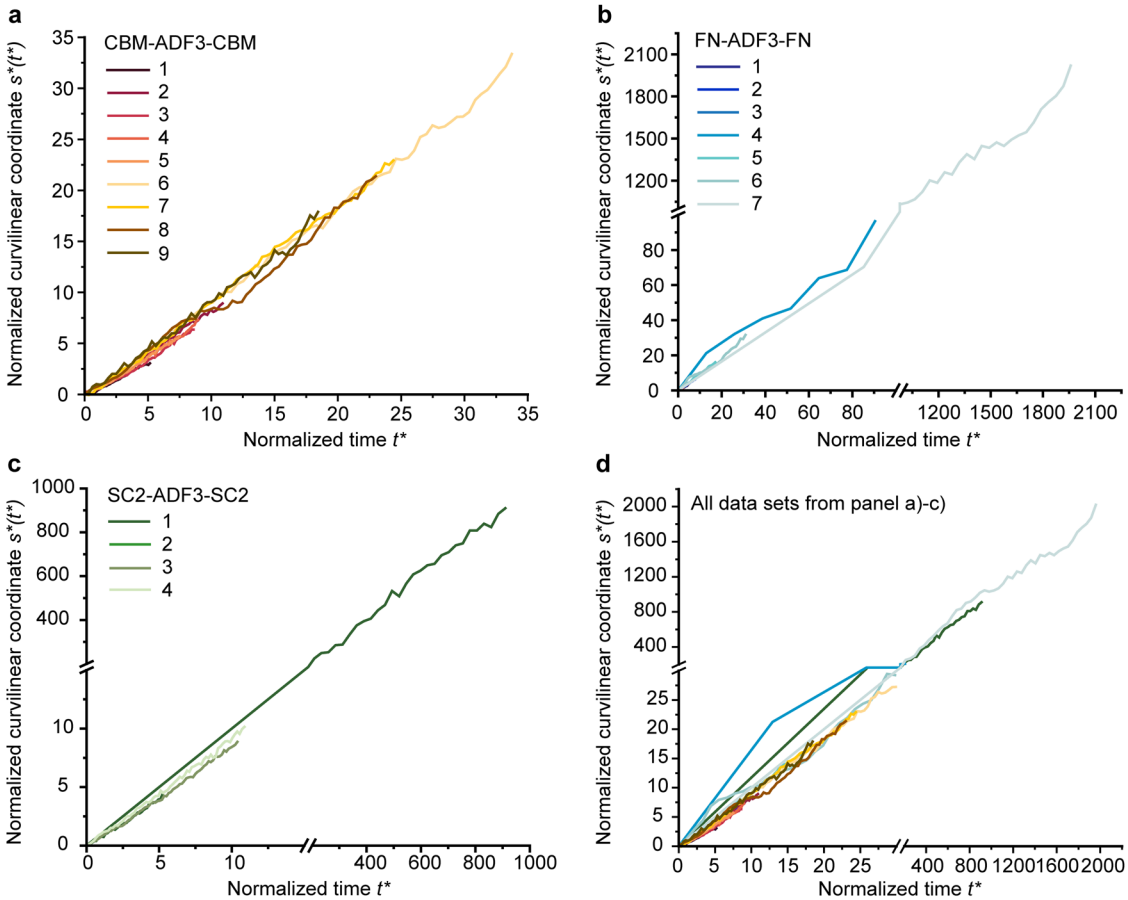

Fig. 7 | Normalized curvilinear coordinate of condensates. Dimensionless plot of the data after normalization by r_c (Eq. 17) for (**a**) Bursting CBM-ADF3-CBM condensates ($n = 9$). Data set 1–9 are represented as lines in different shades of yellow-red. **b** Bursting FN-ADF3-FN condensates ($n = 7$). Data set 1–9 are represented as lines in different shades of blue. **c** Bursting SC2-ADF3-SC2 condensates ($n = 4$). Data set 1–9 are represented as lines in different shades of green. **d** Overview plot containing all data from (**a**–**c**) with the same color coding described in (**a**–**c**).

Wilcoxon signed-rank test indicates no difference in η_m, but a significantly higher shell thickness for CBM-ADF3-CBM (220 ± 60 nm, $n = 9$, rank=a) and FN-ADF3-FN (270 ± 80 nm, $n = 7$, rank=a) compared to SC2-ADF3-SC2 (80 ± 10 nm $n = 4$, rank=b) ($p < 0.05$). The mean ratio of the "bulk" membrane viscosity to bulk viscosity is therefore 130 ± 30 ($n = 9$) for CBM-ADF3-CBM, 200 ± 143 ($n = 7$) for FN-ADF3-FN and 12 ± 6 ($n = 4$) for SC2-ADF3-SC2.

To investigate the effect of the midblock on the biophysical properties of the condensates, we performed micropipette aspiration with CBM-AQ12-CBM. The engineered AQ12 midblock is comparable in size (46.5 kDa) to the ADF3 midblock (43 kDa) but has a more regular sequence consisting of 12 Ala-rich and Gln-rich stretches[34]. In contrast to CBM-ADF3-CBM condensates which readily burst during micropipette aspiration only 2 out of 19 aspirated CBM-AQ12-CBM condensates burst (Supplementary Movie 7, 8). Since bursting of these two CBM-AQ12-CBM condensates started directly at the beginning of the aspiration, data analysis was not possible. The CBM-AQ12-CBM condensates have a five times higher surface tension (19.1 ± 2.2 μN m^{-1}, $n = 17$, rank=b) and surface viscosity (53.2 ± 9.3 μN s m^{-1}, $n = 17$, rank=b) compared to the CBM-ADF3-CBM condensates (rank=a) (Table 1, Fig. 6c). The higher surface tension obtained for CBM-AQ12-CBM, indicates that the condensates are more cohesive and is significant according to the conducted Wilcoxon signed-rank test ($p < 0.05$). As the energy of nucleation of a hole in a shell is inversely proportional to the shell surface tension, it explains also why they burst at the beginning of the aspiration. The high surface viscosity is characteristic of the glassy or nearly glassy state of these condensates which explains why they rarely burst.

Discussion

Knowledge about the biophysical properties of spider silk condensates will help to understand fiber formation as well as condensate-substrate interactions when applied as adhesives. In this work, the biophysical properties of a set of five spider silk protein condensates were determined using micropipette aspiration. Often bursting of condensates was observed during aspiration indicating that they must have a shell formed by protein adsorption at the interface between the dense and dilute phases (Fig. 8a). Aspiration of a condensate with a shell increases the surface tension of the shell (Fig. 8b), which decreases the energy barrier to form a hole, eventually leading to bursting (Fig. 8c). We extracted the surface viscosity and the bulk viscosity from the aspiration and the bursting curves of the condensates using our theoretical model, which combines the physical models for the bursting of viscous bubbles[39] and the dewetting of a liquid film deposited on a liquid substrate[38]. From the measurement of the size of the rim surrounding the hole, we estimate the shell thickness.

The biophysical properties of the condensates studied here are sensitive to the architecture of the protein. They seem to depend on the balance between the dimerization strength of the terminal block and the sticker interactions of the intrinsically disordered midblocks as well as the characteristics of the terminal blocks, i.e., net charge. The dissociation constants K_d of the terminal blocks were previously determined by AUC: CRY = 2.8 μM CBM = 90 μM, FN = 2.3 mM, and no association for SC2[43]. The K_d

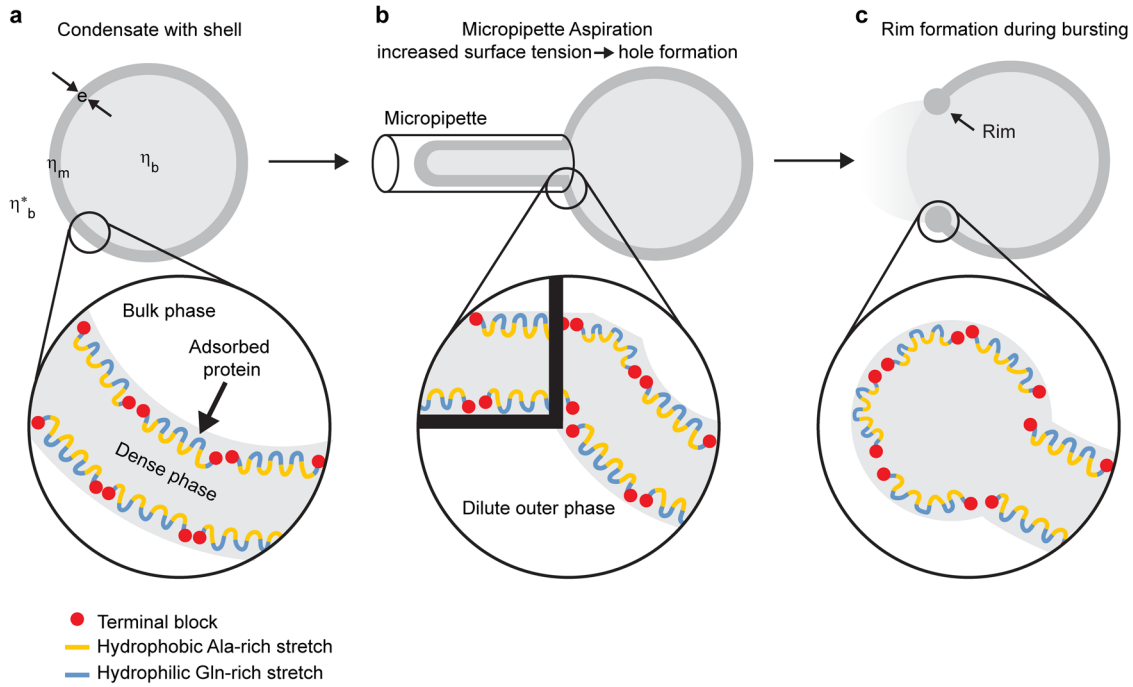

Fig. 8 | Schematic representation of a bursting condensate. a The shell of thickness 100–300 nm may be formed by adsorption of the proteins at the interface between dense and dilute phase coupled to a thermodynamic instability. Since the proteins are amphiphilic the hydrophilic (blue) Gln-stretches may be facing towards the dilute phase while the hydrophobic (yellow) Ala-stretches may face towards the dense phase. **b** Aspiration of the condensate induces the formation of a hole leading to bursting. **c** A rim is formed during bursting. Shell thickness and molecules are not drawn to scale. For illustrational clarity a schematic representation of the silk molecule with a smaller number of Ala-rich and Gln-rich stretches than the real silk molecule (12 stretches each) has been chosen.

of the terminal blocks was found to be related to the concentration of the spider silk proteins required to induce condensate formation[43]. Similarly, the CRY-ADF3-CRY condensates studied here exhibited the highest stability (no bursting), while CBM-ADF3-CBM, FN-ADF3-FN, and SC2-ADF3-SC2 samples contained bursting condensates. We hypothesize that for CRY-ADF3-CRY the high dimerization strength of the end group increases chain length and colocalization of the proteins, which may increase interactions in the midblock. This may be responsible for the increased cohesion of CRY-ADF3-CRY and the formation of a shell that does not burst during micropipette aspiration.

The surface viscosities of the spider silk condensates are 9–68 μN s m^{-1} and in the same order of magnitude as that of PEO-b-PBD polymersomes[55]. For polymersomes the surface viscosities span a wide range from 0.002–8 mN s m^{-1} depending on the block copolymer used[55]. The bulk viscosity of the bursting condensates is lower for CBM-ADF3-CBM and FN-ADF3-FN and higher for SC2-ADF3-SC2. SC2-ADF3-SC2 also shows the highest values for the surface tension, surface viscosity, and shell viscosity (Table 1). In agreement with our results, Fedorov et al.[43] found that the diffusion coefficient of the spider silk protein condensates was lowest in SC2-ADF3-SC2 indicating a high viscosity. This may seem contradictory as the SC2 end groups show no dimerization and should therefore allow fast molecular movement of the silk proteins in the condensate and the shell. However, this behavior can be explained by the biophysical character of SC2-ADF3-SC2. The SC2 terminal blocks are negatively charged resulting in charge repulsion. Thus, the LLPS and properties of the SC2-ADF3-SC2 condensates are based on the multivalent short-range interactions of the intrinsically disordered midblock. Similarly, ref. 56 reported the formation of protein precipitates based on short-range attractive forces in the presence of long-range repulsive forces for lysozyme. In CBM-ADF3-CBM and FN-ADF3-FN, both end group dimerization and interactions in the midblock contribute to the biophysical properties of the condensate. This is also reflected by the same rank (a) of the two protein condensates in the Wilcoxon signed-rank test ($p < 0.05$) for surface viscosity, bulk viscosity, shell viscosity, and shell thickness.

The shell thickness e cannot be deduced from the ratio of the surface viscosity to the bulk viscosity. However, e can be estimated by measuring the radius of the rim of the bursting condensates and is in the order of 100–300 nm. Thus, the shell of silk protein condensates appears to be thinner than the 1–2 μm shells of previously reported core-shell nucleo-protein-RNA condensates[26,31] and protein-based condensates with a shell[25,30] but thicker than the shell of polymersomes, which range from 1 to 21 nm[15–17]. Mechanically stable capsules made from spider silk protein by interfacial absorption or emulsification are reported to have a thin shell of 50–70 nm[57,58]. The larger shell thickness obtained in this work may be the result of the condensate spinodal instability, resulting from a strong protein adsorption at the condensate surface and a protein depletion in the condensate center. However, the bulk viscosity measurements show that the protein solution is concentrated inside the condensate.This is inconsistent with the spinodal decomposition model, which would lead to thicker shells enclosing dilute solution. We postulate that the system may be close to a thermodynamic instability leading to a thick adsorbed layer.

Condensate bursting is influenced by the midblock. More bursting events are observed with the native ADF3 midblock compared to the engineered AQ12 midblock. Both midblocks are intrinsically disordered, similar in length, and amphiphilic in character with hydrophobic Ala-rich stretches and hydrophilic glycine- and Gln-rich stretches. It has been reported by Kelley et al.[59] that amphiphilic peptides can act as surfactants and form shells at the condensate interface. In the spider silk fiber the Ala-rich stretches have a β-sheet structure, whereas the glycine- and Gln-rich stretches adopt more flexible β-spirals, β-turns, and 3_1-helices[60]. In the solution state the Ala-rich stretches of the silk protein form short α-helices. Since AQ12 was derived from ADF3, both proteins have a similar amino acid composition (ADF3: 13.7% Ala, 19.8% Gln, 38.5% Gly; AQ12: 13.6% Ala, 22.7% Gln, 36.4% Gly)[36]. However, the multivalent inter protein interactions, such as π-π stacking or hydrophobic interactions, as well as regions with secondary structures may be more regular for the highly repetitive AQ12 than the native ADF3 midblock. Thus, the AQ12 midblock

may be more amphiphilic and form a more regular shell, resulting in less frequent bursting events.

The formation of a protein shell at the water-air interface has previously been reported for a hanging drop containing CBM-AQ12-CBM condensates. Mohammadi et al.[61] found an increase in the β-sheet content of the silk protein in the dried shell using wide angle X-ray scattering and Raman spectroscopy. The increase in β-sheet content of spider silk proteins at interfaces has also been exploited to form capsules with thin shells by interfacial absorption or emulsification which can function as compartments for enzymatic reactions[57,58]. Furthermore, Välisalmi et al.[42] reported the formation of hydrophobic silk films on glass upon deposition and drying of the spider silk proteins also used in this study. X-ray photoelectron spectroscopy (XPS) revealed that the hydrophobic Ala-rich stretches of the midblock are exposed at the air-water interface and that this conformation is maintained during drying resulting in a hydrophobic film[42]. In contrast, in the condensates studied here the more hydrophilic terminal blocks and Gln-rich stretches of the spider silk proteins may be exposed at the interface between the dense and dilute phases while the Ala-rich stretches may be mostly directed towards the interior of the shell (Fig. 8). This leads to a more ordered conformation of the proteins at the interface and the formation of a protein shell. Similar multiphase condensates of a single protein component have been proposed by Garaizar et al.[27] for fused in sarcoma (FUS) protein condensates during ageing. In the FUS condensates the proteins in the shell exhibit a higher cross-β-sheet content than the proteins in the core.

Conclusion

The physical model developed in this work lays the foundation to obtain the rheological properties of bursting shell-forming condensates. We hypothesize that shell formation is induced by silk protein adsorption at the interface between the dense and dilute phase. The terminal blocks as well as the midblock affect shell stability and bursting behavior of the condensates. Future work will focus on determining the conformation of the proteins in the shell and investigating the effects of salts, pH, temperature, and pressure on bursting. We anticipate that the ability to control and induce the bursting of condensates will enable their use as containers for controlled release of contained cargo, biochemical reaction products, and the tuning of material formation processes.

Methods

Spider silk proteins constructs

The spider silk proteins used in this work were constructed using a cloning procedure described previously[34]. The protein sequences can be found in the Supplementary Data 1.

Protein expression and purification

The protein expression was performed in *E. coli* BL21 (DE3) (ThermoFisher Scientific) using EnPresso media according to the protocol of the manufacturer (EnPresso B 500, EnPresso GmbH) at 30 °C. After 24 h of induction with Isopropyl β-d-1-thiogalactopyranoside (IPTG, final concentration 200 μM) the cells were harvested (12,000 g for 15 min) and resuspended in 50 mM Tris/HCl buffer pH 7.4 containing 3 mM $MgCl_2$, 100 mM NaCl, 1 mg ml^{-1} Lysozyme (EC 3.2.1.17, Merck), 20 μg ml^{-1} DNAse I (EC 3.1.21.1, Merck) and 1 protease inhibitor tablet/100 ml buffer (SIGMA-FAST™ Protease Inhibitor Cocktail Tablets, EDTA-Free, Merck). The resuspended cells were incubated for 1 h at room temperature (RT) and 150 rpm followed by sonication (Qsonica 500, Qsonica LLC), for 3 × 1 min with 40% amplitude. The lysate was centrifuged at 25,200 *g* for 30 min at RT and the supernatant was collected. The proteins were purified by heat treatment at 65 °C for 20 min for CBM-ADF3-CBM or at 70 °C for 30 min for all other proteins. The precipitated proteins were removed with 2 × 15 min centrifugation (3200 g) and the supernatant containing the purified spider silk protein was collected. The buffer was exchanged with deionised water after purification using Econo-Pac 10DG gel filtration columns (Bio-Rad Inc.). The protein solution was frozen in liquid nitrogen and stored at −80 °C until further use.

Protein purity and identity was confirmed with sodium dodecyl polyacrylamide gel electrophoresis using a 10% Mini-PROTEAN TGX precast protein gel (Bio-Rad) and precision plus dual color protein standard (Bio-Rad). The electrophoresis was performed for 90 min at constant 110 V and about 40 mA. To visualize the proteins, the gel was stained with Coomassie brilliant blue R-250 for 1 h and destained with a solution containing 48% acetic acid and 40% ethanol for several hours before imaging.

Condensate formation

For sample preparation 20 ml of the protein solution was concentrated in centrifugal concentrators (30 kDa cut-off) with a poly(ether sulfone) membrane (Viaspin, Satorius AG) at RT 1200 xg. LLPS of the protein was monitored by optical microscopy (Zeiss Axio Vert A1, Carl Zeiss AG). The condensate-containing sample (100–500 μl) was collected for micropipette aspiration and the concentration of the samples was measured with amino acid analysis (see Amino acid analysis section below). The protein concentration of the samples was in the range of 0.6–1.7 mM depending on the protein (see Table 1).

Time stability and coalescence

The stability and coarsening of the samples collected and stored in 1.5 ml tubes at RT was followed over time. At each time point after sample preparation the sample in the tube was mixed and 2 μl of sample were imaged using an optical microscope (Zeiss Axio Vert A1, Zen 2.3 (version 2.3.69.1000)) equipped a 40x/0.6 Ph2 objective lens and an AxioCam 503 colour camera. We analysed movies of the coalescence of the condensates to monitor if they remain liquid or become glassy using Fiji (ImageJ 1.52p). The coalescing of condensates with a shell can be studied using simple scaling arguments. We expect two regimes: If $\eta_s = \eta_m e$ is larger than $\eta_b R_0$ or R_0 smaller than r_c (Eq. 10) the area of fusion A_f is proportional to $R_0^2 \frac{\gamma}{\eta_b} t$. In the regime where R_0 is larger than r_c, A_f is given by the classical Frenkel law which yields the capillary velocity, defined by the ratio of the surface tension γ over the bulk viscosity η_b. For $R_0 < r_c$ the coalescence time increase quadratically with respect to R_0 and for $R_0 > r_c$ the coalescence time increase linearly with R_0 (Supplementary Fig. 6).

Micropipette aspiration

Micropipette aspiration was performed using pulled (PN-31, Narishige) borosilicate capillaries (WPI, 1 mm/0.5 mm outer/inner diameter). The micropipettes were sized to a typical radius of 10–20 μm and bent using a microforge (MF-900, Narishige) to allow for horizontal insertion of the micropipette into the observation chamber. To control the pressure during the experiment and to fill the micropipette with water, it was attached to a tubing connected to a piezoelectric pressure controller (OB1 Mk3, Elveflow). The zero pressure of the micropipette was determined before each experiment. Pressure was applied using the pressure controller so that there is no pressure difference at the entry of the pipette. For the in-house build setup used here the vertical distance h between the water tank and the sample chamber is about 35 cm, resulting in a zero pressure of about 3.5 kPa. The measurement chambers were composed of two glass coverslips spaced by 4 layers of parafilm to provide a 1 mm gap and filled with the condensate-containing sample (5–10 μl). The chamber was sealed with a small amount of oil (Immersol 518 F, Carl Zeiss) to prevent evaporation. All experiments were performed at room temperature. At first a small amount of dilute phase was aspirated. After bringing the micropipette of radius R_p into contact with a condensate of radius R_0 the aspiration of the condensate was performed by applying a constant negative suction pressure ΔP. The pressure was then released and the relaxation of the condensate was monitored. When bursting occurred in some cases only the aspiration of the condensate could be followed since the busting took place already during aspiration. Bright field images of the process were acquired with a time interval of 0.1–1 s using a Nikon Eclipse Ti inverted microscope (Nikon) operated by micromanager (2.0, beta version) with a Zyla sCMOS camera (Andor). The critical pressure (ΔP_c) of the condensate was determined by stepwise increasing the suction

pressure until the condensate would start to enter the micropipette before the aspiration if possible. Different condensates from the sample preparation were measured for CRY-ADF3-CRY and CBM-ADF3-CBM. For FN-ADF3-FN, SC2-ADF3-SC2 and CBM-AQ12-CBM different condensates from two to three sample preparations were aspirated. The data analysis was performed in Fiji (ImageJ 1.52p) using the manual tracking plugin to measure the aspiration and retraction length. The bursting radius, the curvilinear coordinate, the rim radius, and the angular coordinate of the condensates were evaluated using the measure function of ImageJ. Linear fits were performed in Microsoft Excel (Microsoft 365 2021–2024) and the fit of the curvilinear coordinate was performed in OriginPro 10.0.0.154 (Academic). To test for statistical differences between the calculated biophysical properties of the different silk protein condensates a post-hoc Wilcoxon signed-rank test was conducted, both with and without Holm's p-value correction in R (R 4.3.3). The results are summarized in a compact letter display considering p values of less than 0.05 as significant (Fig. 5). The Holm's p value correction was applied to mitigate the risk of inflated Type I error (false positive) rates resulting from multiple comparisons. However, the reported ranks in the results section are derived from non-corrected p values because the sensitivity of the statistical test declines when applying the p value correction. The reason for this is the small sample sizes. The ranks with Holm's p value correction, together with corrected and non-corrected p values are reported in Supplementary Data 3. Additionally, effect sizes and confidence intervals are presented in Supplementary Data 3. Effect sizes for each comparison are expressed as Cliff's delta, where positive values suggest that group 1 likely yields larger values than group 2, and negative values imply the opposite. The magnitude of the difference can be interpreted as negligible for $|\text{value}| < 0.147$, small for $|\text{value}| < 0.33$, medium for $|\text{value}| < 0.474$, and otherwise large[62]. Additionally, 95% confidence intervals are provided for Cliff's delta.

Amino acid analysis

The protein concentration of the samples was determined using amino acid analysis. The original sample was diluted 10-fold and hydrolyzed in 6 M HCl (Merck), containing 0.1% phenol (Sigma-Aldrich) at 110 °C for 24 h under nitrogen atmosphere. L-norleucine (Sigma-Aldrich) was used as an internal standard. The acid was evaporated and the sample was resuspended according to the system protocol (Sykam GmbH). The sample was analysed using an amino acid analyser (S433, Sykam GmbH) equipped with a UV detector at 570 nm and 440 nm. The protein amount was quantified based on the internal standard and the sequence of the protein. Since the most abundant and thus most reliable amino acids in the protein are alanine, glycine, glutamine, and glutamic acid, these amino acids were used for the concentration determination.

Reporting summary

Further information on research design is available in the Nature Portfolio Reporting Summary linked to this article.

Data availability

All datasets are available online on the zenodo.org platform[63]: https://doi.org/10.5281/zenodo.8337749. Representative movies for the aspiration and bursting are available as Supplementary Movie 1–8. All protein sequences are provided as Supplementary Data 1. Details on the statistical test are available in Supplementary Data 2. All obtained values from the micropipette aspiration are available as Supplementary Data 3. Supplementary Information is available online.

Received: 13 October 2023; Accepted: 2 May 2024;
Published online: 17 May 2024

References

1. Alberti, S. & Hyman, A. A. Biomolecular condensates at the nexus of cellular stress, protein aggregation disease and ageing. *Nat. Rev. Mol. Cell Biol.* **22**, 196–213 (2021).
2. Banani, S. F., Lee, H. O., Hyman, A. A. & Rosen, M. K. Biomolecular condensates: organizers of cellular biochemistry. *Nat. Rev. Mol. Cell Biol.* **18**, 285–298 (2017).
3. Sun, Y., Lim, Z. W., Guo, Q., Yu, J. & Miserez, A. Liquid–liquid phase separation of proteins and peptides derived from biological materials: discovery, protein engineering, and emerging applications. *MRS Bull.* **45**, 1039–1047 (2020).
4. Rising, A. & Harrington, M. J. Biological materials processing: time-tested tricks for sustainable fiber fabrication. *Chem. Rev.* **123**, 2155–2199 (2023).
5. Michieletto, D. & Marenda, M. Rheology and viscoelasticity of proteins and nucleic acids condensates. *JACS Au* **2**, 1506–1521 (2022).
6. Guevorkian, K., Colbert, M.-J., Durth, M., Dufour, S. & Brochard-Wyart, F. Aspiration of biological viscoelastic drops. *Phys. Rev. Lett.* **104**, 218101 (2010).
7. González-Bermúdez, B., Guinea, G. V. & Plaza, G. R. Advances in micropipette aspiration: applications in cell biomechanics, models, and extended studies. *Biophys. J.* **116**, 587–594 (2019).
8. Sandre, O., Moreaux, L. & Brochard-Wyart, F. Dynamics of transient pores in stretched vesicles. *Proc. Natl Acad. Sci.* **96**, 10591–10596 (1999).
9. Evans, E., Heinrich, V., Ludwig, F. & Rawicz, W. Dynamic tension spectroscopy and strength of biomembranes. *Biophys. J.* **85**, 2342–2350 (2003).
10. Needham, D. & Nunn, R. S. Elastic deformation and failure of lipid bilayer membranes containing cholesterol. *Biophys. J.* **58**, 997–1009 (1990).
11. Aranda-Espinoza, H., Bermudez, H., Bates, F. S. & Discher, D. E. Electromechanical limits of polymersomes. *Phys. Rev. Lett.* **87**, 208301 (2001).
12. Riske, K. A., Knorr, R. L. & Dimova, R. Bursting of charged multicomponent vesicles subjected to electric pulses. *Soft Matter* **5**, 1983–1986 (2009).
13. Mabrouk, E., Cuvelier, D., Brochard-Wyart, F., Nassoy, P. & Li, M.-H. Bursting of sensitive polymersomes induced by curling. *Proc. Natl Acad. Sci.* **106**, 7294–7298 (2009).
14. Diguet, A. et al. UV-induced bursting of cell-sized multicomponent lipid vesicles in a photosensitive surfactant solution. *J. Am. Chem. Soc.* **134**, 4898–4904 (2012).
15. Discher, B. M. et al. Polymersomes: tough vesicles made from diblock copolymers. *Science* **284**, 1143–1146 (1999).
16. Discher, D. E. & Eisenberg, A. Polymer vesicles. *Science* **297**, 967–973 (2002).
17. Bermudez, H., Brannan, A. K., Hammer, D. A., Bates, F. S. & Discher, D. E. Molecular weight dependence of polymersome membrane structure, elasticity, and stability. *Macromolecules* **35**, 8203–8208 (2002).
18. Mao, S., Kuldinow, D., Haataja, M. P. & Košmrlj, A. Phase behavior and morphology of multicomponent liquid mixtures. *Soft Matter* **15**, 1297–1311 (2019).
19. Bauermann, J., Bartolucci, G., Boekhoven, J., Weber, C. A. & Jülicher, F. Formation of liquid shells in active droplet systems. *Phys. Rev. Res.* **5**, 043246 (2023).
20. Bergmann, A. M. et al. Liquid spherical shells are a non-equilibrium steady state of active droplets. *Nat. Commun.* **14**, 6552 (2023).
21. Saleh, O. A., Wilken, S., Squires, T. M. & Liedl, T. Vacuole dynamics and popping-based motility in liquid droplets of DNA. *Nat. Commun.* **14**, 3574 (2023).
22. West, J. A. et al. Structural, super-resolution microscopy analysis of paraspeckle nuclear body organization. *J. Cell Biol.* **214**, 817–830 (2016).
23. Feric, M. et al. Coexisting liquid phases underlie nucleolar subcompartments. *Cell* **165**, 1686–1697 (2016).
24. Yu, H. et al. HSP70 chaperones RNA-free TDP-43 into anisotropic intranuclear liquid spherical shells. *Science* **371**, eabb4309 (2021).

25. Gallego, L. D. et al. Phase separation directs ubiquitination of gene-body nucleosomes. *Nature* **579**, 592–597 (2020).
26. Kaur, T. et al. Sequence-encoded and composition-dependent protein-RNA interactions control multiphasic condensate morphologies. *Nat. Commun.* **12**, 872 (2021).
27. Garaizar, A. et al. Aging can transform single-component protein condensates into multiphase architectures. *Proc. Natl Acad. Sci.* **119**, e2119800119 (2022).
28. Gennes, P. G. D. *Scaling Concepts in Polymer Physics,* (Cornell Univeristy Press, 1979).
29. Choi, H. et al. Spontaneous transition of spherical coacervate to vesicle-like compartment. *Adv. Sci.* **11**, 2305978 (2024).
30. Chen, N., Zhao, Z., Wang, Y. & Dimova, R. Resolving the mechanisms of soy glycinin self-coacervation and hollow-condensate formation. *ACS Macro Lett.* **9**, 1844–1852 (2020).
31. Alshareedah, I., Moosa, M. M., Raju, M., Potoyan, D. A. & Banerjee, P. R. Phase transition of RNA−protein complexes into ordered hollow condensates. *Proc. Natl Acad. Sci.* **117**, 15650–15658 (2020).
32. Frenkel, J. Viscous flow of crystalline bodies under the action of surface tension. *J. Phys.* **9**, 385 (1945).
33. Batys, P. et al. Self-assembly of silk-like protein into nanoscale bicontinuous networks under phase-separation conditions. *Biomacromolecules* **22**, 690–700 (2021).
34. Mohammadi, P. et al. Phase transitions as intermediate steps in the formation of molecularly engineered protein fibers. *Commun. Biol.* **1**, 86 (2018).
35. Huemmerich, D. et al. Novel assembly properties of recombinant spider dragline silk proteins. *Curr. Biol.* **14**, 2070–2074 (2004).
36. Huemmerich, D. et al. Primary structure elements of spider dragline silks and their contribution to protein solubility. *Biochemistry* **43**, 13604–13612 (2004).
37. Basak, A. et al. High-resolution X-ray crystal structures of human γD Crystallin (1.25Å) and the R58H Mutant (1.15Å) associated with aculeiform cataract. *J. Mol. Biol.* **328**, 1137–1147 (2003).
38. Tormo, J. et al. Crystal structure of a bacterial family-III cellulose-binding domain: a general mechanism for attachment to cellulose. *EMBO J.* **15**, 5739–5751 (1996).
39. Leahy, D. J., Aukhil, I. & Erickson, H. P. 2.0 Å crystal structure of a four-domain segment of human fibronectin encompassing the RGD loop and synergy region. *Cell* **84**, 155–164 (1996).
40. Keeble, A. H. et al. Evolving accelerated amidation by SpyTag/SpyCatcher to analyze membrane dynamics. *Angew. Chem. Int. Ed.* **56**, 16521–16525 (2017).
41. Zakeri, B. et al. Peptide tag forming a rapid covalent bond to a protein, through engineering a bacterial adhesin. *Proc. Natl Acad. Sci.* **109**, E690–E697 (2012).
42. Välisalmi, T., Roas-Escalona, N., Meinander, K., Mohammadi, P. & Linder, M. B. Highly hydrophobic films of engineered silk proteins by a simple deposition method. *Langmuir* **39**, 4370–4381 (2023).
43. Fedorov, D. et al. Triblock Proteins with Weakly Dimerizing Terminal Blocks and an Intrinsically Disordered Region for Rational Design of Condensate Properties. *Small*, 2306817. https://doi.org/10.1002/smll.202306817 (2023).
44. Mabrouk, E. et al. Formation and material properties of giant liquid crystal polymersomes. *Soft Matter* **5**, 1870–1878 (2009).
45. Guyon E., Hulin J.-P., Petit L. & C. D. M. *Physical Hydrodynamics*. (Oxford University Press, 2015).
46. Dragan, Z. An infinite-series solution for the creeping motion through an orifice of finite length. *J. Fluid Mech.* **115**, 505–523 (1982).
47. Piroird, K., Clanet, C. & Quéré, D. Capillary extraction. *Langmuir* **27**, 9396–9402 (2011).
48. Kim, D. H., Costello, M. J., Duncan, P. B. & Needham, D. Mechanical properties and microstructure of polycrystalline phospholipid monolayer shells: novel solid microparticles. *Langmuir* **19**, 8455 (2003).
49. Debrégeas, G., Martin, P. & Brochard-Wyart, F. Viscous bursting of suspended films. *Phys. Rev. Lett.* **75**, 3886 (1995).
50. Brochard-Wyart, F., Debregeas, G., Fondecave, R. & Martin, P. Dewetting of supported viscoelastic polymer films: birth of rims. *Macromolecules* **30**, 1211–1213 (1997).
51. Martin, P., Buguin, A. & Brochard-Wyart, F. Bursting of a liquid film on a liquid substrate. *Europhys. Lett.* **28**, 421–426 (1994).
52. Debrégeas, G., de Gennes, P.-G. & Brochard-Wyart, F. The life and death of bare viscous bubbles. *Science* **279**, 1704–1707 (1998).
53. Brochard-Wyart, F., de Gennes, P. G. & Sandre, O. Transient pores in stretched vesicles: role of leak-out. *Phys. A Stat. Mech. Appl.* **278**, 32–51 (2000).
54. Brochard-Wyart, F., Martin, P. & Redon, C. Liquid/liquid dewetting. *Langmuir* **317**, 1539–1541 (1993).
55. Dimova, R., Seifert, U., Pouligny, B., Förster, S. & Döbereiner, H. G. Hyperviscous diblock copolymer vesicles. *Eur. Phys. J. E* **7**, 241–250 (2002).
56. Stradner, A. et al. Equilibrium cluster formation in concentrated protein solutions and colloids. *Nature* **432**, 492–495 (2004).
57. Blüm, C., Nichtl, A. & Scheibel, T. Spider silk capsules as protective reaction containers for enzymes. *Adv. Funct. Mater.* **24**, 763–768 (2014).
58. Hermanson, K. D., Huemmerich, D., Scheibel, T. & Bausch, A. R. Engineered microcapsules fabricated from reconstituted spider silk. *Adv. Mater.* **19**, 1810–1815 (2007).
59. Kelley, F. M., Favetta, B., Regy, R. M., Mittal, J. & Schuster, B. S. Amphiphilic proteins coassemble into multiphasic condensates and act as biomolecular surfactants. *Proc. Natl Acad. Sci.* **118**, e2109967118 (2021).
60. Anton, A. M. et al. Foundation of the outstanding toughness in biomimetic and natural spider silk. *Biomacromolecules* **18**, 3954–3962 (2017).
61. Mohammadi, P., Zemke, F., Wagermaier, W. & Linder, M. B. Interfacial crystallization and supramolecular self-assembly of spider silk inspired protein at the water-air interface. *Materials* **14**, 4239 (2021).
62. Romano, J., Kromrey, J. D., Corraggio, J. & Skowronek, J. Appropriate statistics for ordinal level data: should we really be using t-test and Cohen's d for evaluating group differences on the NSSE and other surveys? In *Annual meeting of the Florida Association of Institutional Research* 1–3 (2006).
63. Tunn, I. et al. Data for the publication: Bursting of condensates. https://doi.org/10.5281/zenodo.8337749 (2024).

Acknowledgements

The authors thank Mikko Haataja, Maria Sammalkorpi, Alberto Scacchi, Joachim Weber, and the Institut Curie active matter group for helpful discussions. We thank Ellinor Englund for cloning one of the constructs. This work was funded by the Academy of Finland (Projects 346105, 346112), the Center of Excellence Program (2022–2029) in Life-Inspired Hybrid Materials (LIBER), and the Novo Nordisk Foundation (NNF20OC0061306) and the Institute Curie Pierre Sens UMR 168.

Author contributions

I.T., G.B., and M.B.L. conceptualized and designed experiments. I.T. performed sample preparation, experiments, and data analysis. G.B. performed micropipette aspiration experiment and contributed to data analysis and interpretation. J.T. performed amino acid analysis. T.V. performed statistical test and contributed to data interpretation. F.B.W. developed the physical model for data analysis and contributed to data interpretation. J.V.I.T. contributed to setting up the micropipette aspiration method and data interpretation. I.T. and F.B.W. wrote the first draft of the manuscript. All authors contributed to revising the manuscript. M.B.L. finalized the manuscript.

Competing interests
The authors declare no competing interests.

Additional information
Supplementary information The online version contains supplementary material available at https://doi.org/10.1038/s42005-024-01650-5.

Correspondence and requests for materials should be addressed to Françoise Brochard-Wyart or Markus B. Linder.

Peer review information *Communications Physics* thanks the anonymous reviewers for their contribution to the peer review of this work. A peer review file is available.